RSC Advances

PAPER

View Article Online
View Journal | View Issue

Cite this: *RSC Adv.*, 2026, **16**, 6985

Synergistic NIR-polydopamine nanotherapy for blood–brain barrier crossing and Parkinson's disease intervention

Xueer Xia, †[ab] Jianbang Han,†[c] Meiyin Lin,†[d] Yingfeng Tu, [e] Yue Zheng,[f] Bin Liu,[g] Yu Chen,[h] Xin Li,[d] Zirong Zhang,[f] Shuai Han,[i] Wenting Shang,[j] Xiazi Huang‡*[a] and Jianhua Liu ‡*[dk]

Despite its clinical success, conventional deep-brain stimulation (DBS) for Parkinson's remains limited by its invasive nature. To overcome this, we engineered ZnO@polydopamine (ZnO@PDA) nanocomposites as a non-invasive neurotherapeutic platform. By leveraging rational nanostructure design, ZnO@PDA enabled reversible blood–brain barrier (BBB) opening *via* a photothermal mechanism, thereby permitting targeted nanoparticle delivery. Upon reaching the brain, nanocomposites harness ultrasound-driven electrical stimulation to precisely modulate neuronal circuits, thus offering a groundbreaking alternative to traditional DBS. Simultaneously, their potent antioxidant activity neutralizes reactive oxygen species, suppresses microglial overactivation, and mitigates pathological α-synuclein aggregation. *In vivo* studies demonstrated that laser-triggered ZnO@PDA treatment significantly restored dopaminergic neuronal function and improved motor coordination, whereas ultrasound-based protocols alone were less effective owing to insufficient BBB penetration. Our work presents a "penetration–accumulation–stimulation" cascade strategy, delivering a transformative approach to non-invasive treatment of neurodegenerative disorders.

Received 9th October 2025
Accepted 28th January 2026

DOI: 10.1039/d5ra07719b

rsc.li/rsc-advances

1. Introduction

Parkinson's disease (PD) is a severe and progressive neurodegenerative illness characterized by gradual degeneration of dopaminergic neurons within the substantia nigra of the midbrain,[1] ultimately leading to profound neurological deficits.[2] Recent global burden of disease studies have reported that PD affects more than six million individuals worldwide, making it the fastest-growing neurological condition.[3] Despite significant advancements in early diagnosis and therapeutic interventions,[4] PD remains a formidable clinical challenge owing to its complexity and heterogeneity.

Deep brain stimulation (DBS), an invasive neurosurgical procedure, has long served as a cornerstone therapy, along with pharmacological approaches.[5,6] Nevertheless, its clinical utility is constrained by considerable postoperative complications including intracranial hemorrhage,[7,8] infection,[9] induced seizures,[10,11] mechanical failures,[12,13] and even permanent neurological deficits.[14] This underscores the urgent need for effective and innovative strategies for treating PD.

[a]*Medical Engineering &Engineering Medicine Innovation Center, Hangzhou International Innovation Institute, Beihang University, No. 166, Shuanghongqiao Street, Yuhang District, 311115, Hangzhou, China. E-mail: sharon@buaa.edu.cn; Tel: +86-13580346984*

[b]*Department of General Surgery (Colorectal Surgery), Biomedical Innovation Center, The Sixth Affiliated Hospital, Sun Yat-sen University, Guangzhou, 510655, China*

[c]*Department of Neurology, Guangzhou First People's Hospital, The Second Affiliated Hospital of South China University of Technology, Guangzhou, 510000, China*

[d]*Department of Oncology, Guangdong Provincial People's Hospital (Guangdong Academy of Medical Sciences), Southern Medical University, No. 123 Huifu Road West, Yuexiu District, Guangzhou, 510080, China. E-mail: liujianh80@126.com; Tel: +86-20-18666003180*

[e]*NMPA Key Laboratory for Research and Evaluation of Drug Metabolism & Guangdong Provincial Key Laboratory of New Drug Screening, School of Pharmaceutical Sciences, Southern Medical University, Guangzhou, 510515, China*

[f]*Department of Gastroenterology, Guangdong Provincial People's Hospital (Guangdong Academy of Medical Sciences), Southern Medical University, Guangzhou, 510080, China*

[g]*Department of Radiology, Guangdong Provincial People's Hospital (Guangdong Academy of Medical Sciences), Southern Medical University, Guangzhou, 510080, China*

[h]*Department of Pathology, Guangdong Provincial People's Hospital (Guangdong Academy of Medical Sciences), Southern Medical University, Guangzhou, 510080, China*

[i]*Department of Gastrointestinal Surgery, General Surgery Center, Zhujiang Hospital, Southern Medical University, Guangzhou, 510282, China*

[j]*Institute of Automation, Chinese Academy of Sciences, Beijing, 100190, China*

[k]*Guangdong Provincial People's Hospital Ganzhou Hospital (Ganzhou Municipal Hospital), Ganzhou, Jiangxi, 341000, China*

† These authors contributed equally to this work.

‡ These authors should be considered co-corresponding authors.

Driven by a deeper understanding of the pathogenesis and pathophysiology of PD, non-invasive brain stimulation modalities leveraging ultrasound (US),[15] magnetism,[16] light, and electricity have garnered extensive attention.[17] Recent breakthroughs in nanotechnology have created a new era for the intersection of noninvasive DBS and efficient drug delivery. Pioneering work by Kim *et al.*[18] demonstrated that US-responsive piezoelectric nanoparticles (NPs) could achieve symptomatic relief in PD models, whereas Wu *et al.*[19] reported a photothermally activated wireless DBS nanosystem that enabled near-infrared (NIR)-mediated neuronal stimulation and functional restoration. These advances highlight the transformative potential of multifunctional NPs in overcoming the long-standing therapeutic bottlenecks in PD. Among the various nanomaterials, zinc oxide NPs (ZnO-NPs) have emerged as particularly promising candidates because of their high reactivity, versatility, and neuroprotective effects,[20,21] enabling effective noninvasive DBS under various external stimulations. Concurrently, substantial evidence has indicated that oxidative stress, release of inflammatory mediators, and enhanced immune responses are critical pathophysiological mechanisms driving PD progression.[22,23] Notably, polydopamine (PDA), a melanin-like compound, exhibits potent free-radical-scavenging capacity and immunomodulatory properties that can alleviate cellular damage.[24,25] Based on these findings, we propose a novel core–shell nanocomposite architecture that employs ZnO as the piezoelectric substrate and PDA as the functional coating. This strategy can integrate ultrasonic-mediated noninvasive DBS with concurrent PDA release, thus synergizing neuromodulation with antioxidant, anti-inflammatory, and pharmaceutical effects.

However, effective therapeutic delivery remains challenging because of the formidable blood–brain barrier (BBB), which significantly impedes NPs accumulation in brain tissue.[26,27] Previous studies[28,29] have shown that low-temperature photothermal therapy (PTT, 41–43 °C) using 808 nm NIR can overcome this obstacle, thereby improving therapeutic outcomes. Notably, PDA exhibits exceptional photothermal conversion properties owing to its unique molecular structure,[30,31] facilitating vasodilation and promoting internalization of composite NPs upon NIR exposure. Recently, Gao *et al.*[32] developed a targeted NIR-responsive nanoplatform capable of efficiently traversing the BBB under NIR irradiation, thereby achieving sustained therapeutic effects in PD. These findings highlight the clinical potential of PDA-based NPs, warranting further investigation for their translational implementation.

Inspired by these advances, we herein report the design and synthesis of ZnO@PDA nanocomposites: photothermally activated, US-responsive, piezoelectric NPs with excellent biocompatibility. Following systemic administration, ZnO@PDA efficiently crossed the BBB upon NIR stimulation, enabling its accumulation in the deep brain. Within neuronal environments, particles transduce US stimuli into localized electrical signals, offering a noninvasive DBS alternative. Prior to translational application, we comprehensively characterized the physicochemical properties, photothermal conversion

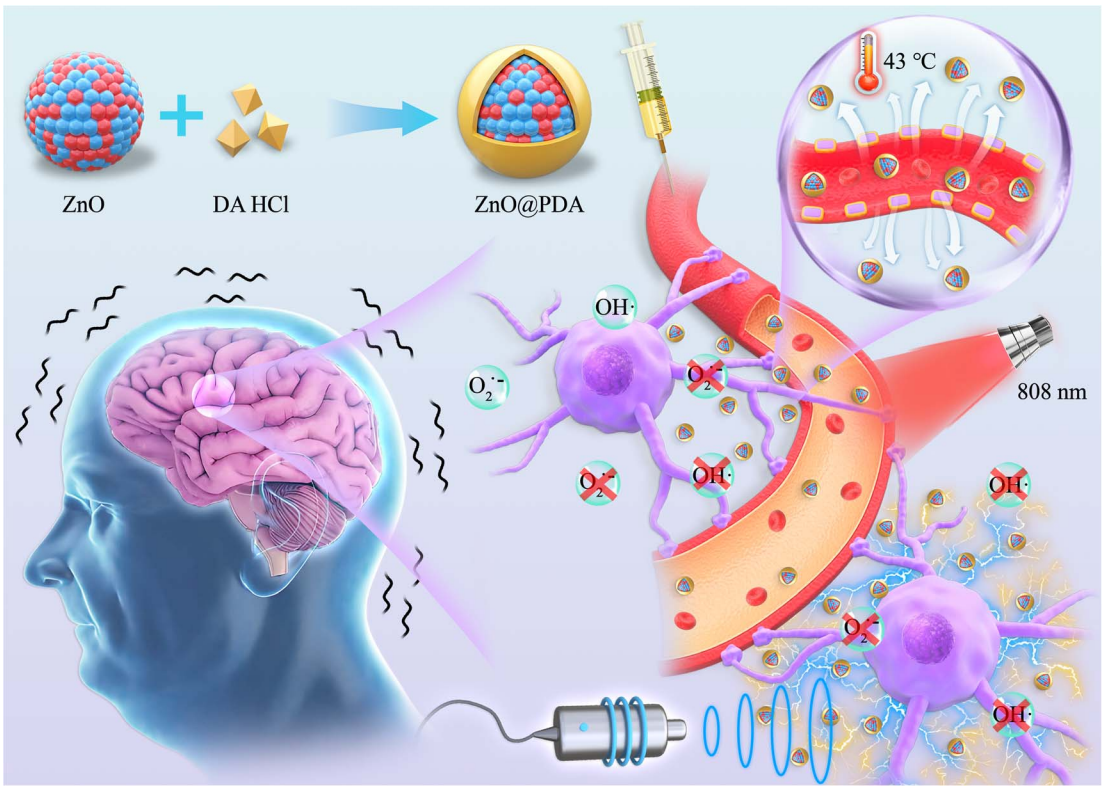

Scheme 1 Schematic preparation of ZnO@PDA and the mechanism of "penetration-accumulation-stimulation" progression of non-invasive deep brain stimulation.

capability, and antioxidant capacity of ZnO@PDA. Furthermore, a series of *in vitro* and *in vivo* evaluations validated their neuroprotective efficacy and therapeutic potential (Scheme 1).

2. Results

2.1. Synthesis and characterization of ZnO@PDA

The successful synthesis of ZnO@PDA NPs *via* the integration of dopamine hydrochloride with ZnO NPs is shown in Fig. 1A. The hydrodynamic diameter and surface charge properties were comprehensively analyzed using dynamic light scattering (DLS) and zeta potential measurements (Fig. 1B and C). Unmodified PDA displayed a hydrodynamic diameter of approximately 40 nm with a neutral surface charge. In contrast, pristine ZnO NPs exhibited significantly larger dimensions (approximately 90 nm) and a positive zeta potential of 32.5 ± 3.3 mV. After coating with PDA, the prepared ZnO@PDA NPs showed a moderate increase in size to approximately 130 nm, with a charge reversal of −15.3 ± 0.2 mV. The smaller hydrated particle size was aligned with its excellent water-dispersion characteristics. Notably, the electronegative properties presented favorable biosafety, enabling prolonged participation in the systemic circulation. The surface modification and functionalization process of NPs can be monitored using Fourier transform infrared (FTIR) spectroscopy, further confirming their affinity. Generally, the characteristic absorption peaks at 400 cm^{-1} and 560 cm^{-1} were assigned to ZnO vibrational modes.[33] Peaks at 1510 cm^{-1} and 1610 cm^{-1} originated from the stretching vibrations of aromatic ν(C=C) and pyrrole/indole ring coupling in PDA, and the peak at 1381 cm^{-1} corresponded to ν(C–N) stretching vibrations in aromatic and indole rings[34] (Fig. 1D). In this study, morphological verification was performed using transmission electron microscopy (TEM) (Fig. 1E), which revealed NP dimensions ranging from 40 to 150 nm. Elemental mapping analysis demonstrated the homogeneous distribution of nitrogen across the NPs, providing direct evidence of the PDA coating on the ZnO surfaces. As evidenced by powder X-ray diffraction (XRD), the crystalline integrity of the ZnO cores was maintained after the PDA coating (Fig. 1F). The diffraction peaks at 31.9°, 34.4°, 36.3°, 47.5°, and 56.6° correspond to the (100), (002), (101), (102), and (110) crystal planes of ZnO, respectively, which is consistent with the characteristic peaks of hexagonal ZnO[33] (JCPDS No. 79-0206). In addition, the X-ray photoelectron spectroscopy (XPS) image and the distinct –C–N peak at 401 eV in the N 1s spectrum further corroborated the effective deposition of PDA onto the ZnO surfaces (Fig. 1G and H).

Collectively, multi-modal characterizations (including morphological, compositional, and crystallographic analyses) confirmed the successful synthesis of ZnO@PDA, exhibiting structural stability, strong affinity, and charge reversal, which are key potentials for an optimal neurological nanoplatform.

2.2. Special properties of ZnO@PDA

Subsequently, the ZnO@PDA platform was evaluated for dual therapeutic functions: noninvasive deep brain electrical stimulation and inflammatory microenvironment (IME) modulation.

To investigate the optical characteristics of ZnO@PDA, ultraviolet-visible (Vis) absorption spectra were acquired for PDA, ZnO, and ZnO@PDA (Fig. 1I). PDA showed broad absorption across the NIR region with a weak peak at approximately 260 nm. As an N-type semiconductor, ZnO exhibits a strong absorption peak at 380 nm, which is attributed to electron transitions from the valence band under UV irradiation.[35] Upon PDA coating, the apparent color of the material changed from white to dark green, accompanied by a slight attenuation of the 380 nm absorption peak. Furthermore, the photothermal conversion efficiency was quantified by monitoring the temperature elevation profiles. As shown in Fig. 1J, ZnO@PDA exhibited concentration- and time-dependent heating, reaching 44.0 ± 0.5 °C at 50 μg mL^{-1} (ΔT > 10 °C *vs.* PBS controls), displaying a mild thermal effect on BBB opening.

Moreover, current-time profiles recorded during 30 s on/off cycles (Fig. 1K) revealed consistent current generation (>0.12 μA) exclusively during US activation periods, with the baseline current remaining below detection limits. This clear switching behavior confirms the US-responsive piezoelectric characteristics of ZnO@PDA. Unlike conventional DBS, which requires invasive electrode implantation, our NPs system enabled neuromodulation through noninvasive electrical stimulation.

Microglia, which serve as the principal immune effector cells in the central nervous system, undergo pathological activation within the substantia nigra and striatum of PD patients,[36] where they aberrantly secrete pro-inflammatory cytokines (TNF-α, IL-1β, and IL-6) and reactive oxygen species (ROS) that collectively drive neuronal degeneration.[37,38] In addition to PD-associated neuroinflammation, ZnO@PDA presented multi-target antioxidant functionality, which was evaluated using three complementary assays. In the 2,2-diphenyl-1-picrylhydrazyl (DPPH) assay, the color of the DPPH solution decayed in a concentration-dependent manner after ZnO@PDA treatment, and the maximum absorption peak at 517 nm was significantly reduced, indicating that ZnO@PDA effectively neutralized the free radicals *via* an electron transfer mechanism (Fig. 1L). The hydroxyl radical (˙OH) scavenging capacity was investigated using 3,3′,5,5′-tetramethylbenzidine (TMB) chromogenic detection, where colorless TMB underwent ˙OH-mediated oxidation to form blue products that were converted to yellow derivatives with maximum absorbance at 450 nm after acidification. Notably, increasing the ZnO@PDA concentration progressively suppressed the spectral absorption intensity at 450 nm (Fig. 1M), which is consistent with the effective ˙OH radical interception. To assess the antioxidant profile, superoxide anion ($O_2^{\bullet -}$) scavenging capability was examined using a WST-8/xanthine oxidase assay. The control group showed strong formazan generation (λ_{max} = 450 nm) *via* superoxide-mediated WST-8 reduction, whereas ZnO@PDA treatment suppressed this chromogenic process in a concentration-dependent manner (Fig. 1N), indicating catalytic superoxide neutralization through PDA-mediated dismutation mechanisms. These experimental findings demonstrated the therapeutic potential of ZnO@PDA in ameliorating IME. Moreover, its stability was

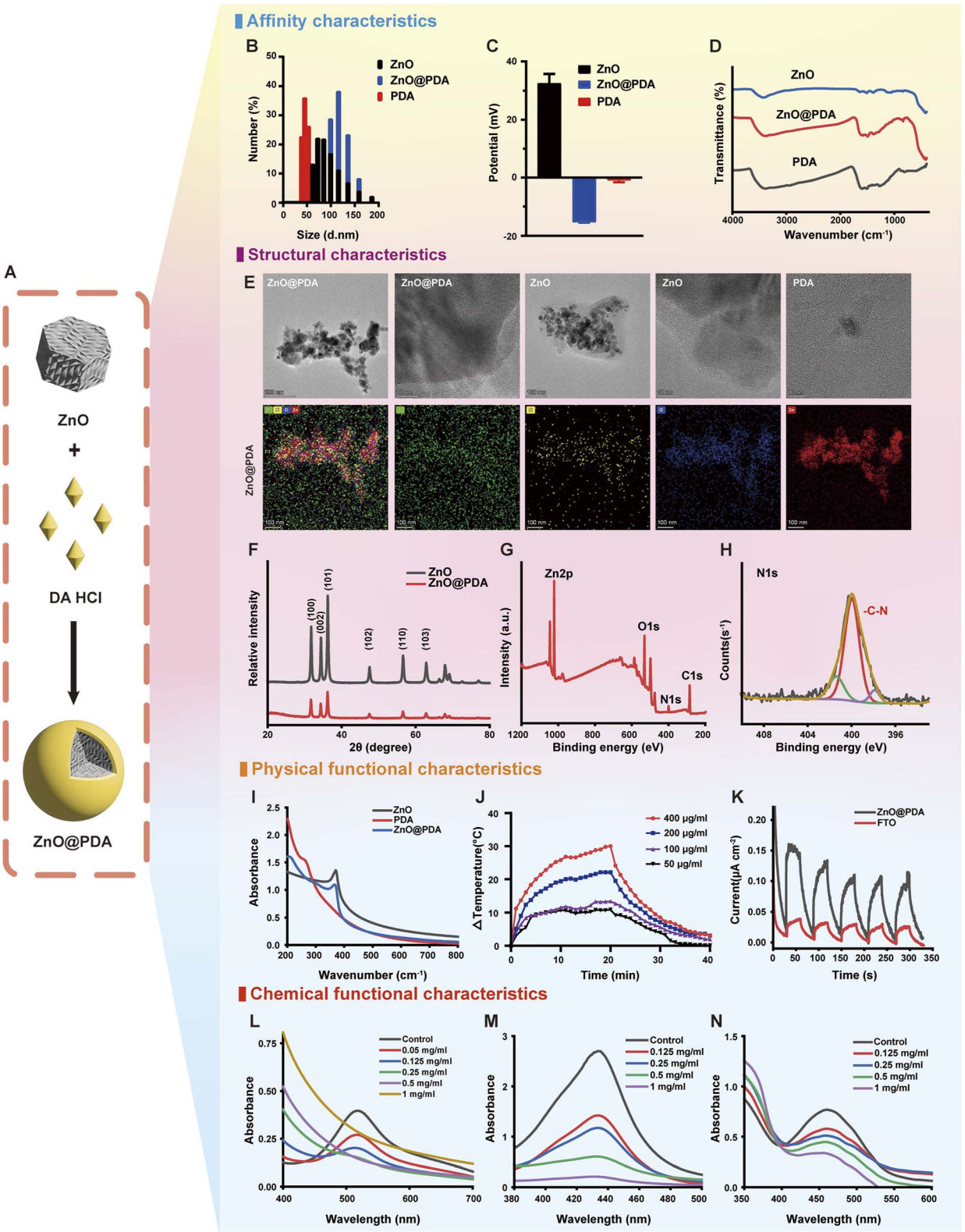

Fig. 1 Special properties of ZnO@PDA. (A) Flow chart for ZnO@PDA preparation. (B) DLS size distribution of ZnO, ZnO@PDA and PDA in water. (C) The zeta potential of ZnO, ZnO@PDA and PDA. (D) FT-IR spectrum of ZnO, ZnO@PDA and PDA. (E) TEM images of as-made ZnO@PDA, ZnO and PDA and the elemental distribution of ZnO@PDA. (F) XRD pattern of ZnO and ZnO@PDA. (G) The high-resolution XPS of ZnO@PDA. (H) The high-resolution XPS of N (1 s). (I) UV-vis absorption of ZnO, ZnO@PDA and PDA. (J) Photothermal conversions of ZnO@PDA with different concentrations under 808 nm laser irradiation (20 min, 1.5 W cm^{-2}), and temperature changes after cessation of irradiation. (K) I–T curves of ZnO@PDA under ultrasound 30 s switching cycle stimulation. (L) DPPH radical scavenging capacity of ZnO@PDA. (M) Hydroxyl radical scavenging capacity of ZnO@PDA. (N) Superoxide anion radical scavenging capacity of ZnO@PDA.

assessed using 72-hour serum incubation experiments. Continuous spectral monitoring showed no significant fluctuations in the intensity of the absorbance peak (SI Fig. 1), confirming its reliable performance.

2.3. *In vitro* experiments with ZnO@PDA

To further validate the multifunctional therapeutic efficacy of ZnO@PDA in neuronal cells, we established a cellular model of PD by treating PC12 cells with 6-hydroxydopamine (6-OHDA) and conducted a series of *in vitro* experiments. CCK-8 assays demonstrated dose-dependent reductions in PC12 cell viability at 0–500 μmol L^{-1} 6-OHDA, with approximately 50% survival observed at 150 μmol L^{-1} ($p < 0.0001$), establishing this concentration for PD modeling. Notably, 200 μg mL^{-1} ZnO@PDA significantly restored cell viability to over 75% ($p < 0.0001$ *vs.* the model group) and could be selected for subsequent experiments (Fig. 2A). As shown in Fig. S2, human umbilical vein endothelial cells (HUVEC) treated with ≤300 μg mL^{-1} ZnO@PDA for 24 hours exhibited over 80% cell viability, indicating that ≤300 μg mL^{-1} is a safe concentration for normal cells. To investigate photothermal effects on NPs internalization, Cy5-conjugated ZnO@PDA were incubated with PC12 cells under NIR irradiation or in the dark. Confocal laser scanning microscopy revealed markedly enhanced cellular uptake of ZnO@PDA upon NIR stimulation ($p < 0.01$ *vs.* dark control) (Fig. 2B and C). In addition, under identical field-of-view sizes, quantification analysis was conducted on the two groups of cells, and the results showed no significant change in cell count ($p > 0.05$), indicating that NIR stimulation could enhance the cellular uptake of the materials without causing obvious cytotoxicity (Fig. 2D). Furthermore, flow cytometric analysis using DCFH-DA fluorescence revealed significantly elevated ROS levels in 6-OHDA-treated PC12 cells, whereas ZnO@PDA with 808 nm NIR irradiation effectively suppressed ROS generation to near-normal levels ($p < 0.001$), demonstrating its ability to protecting neuronal cells from oxidative stress (Fig. 2E and F).

Flow cytometric apoptosis analysis (Fig. 3A) showed a marked increase in the apoptosis rate (68.9%) in 6-OHDA-treated cells (model group) compared to the control group ($p < 0.0001$) (Fig. 3B), while ZnO@PDA treatment alone decreased apoptosis to 59.8% ($p < 0.05$, *vs.* model group). The protective effect was further enhanced under NIR irradiation, which lowered apoptosis to 51.0% ($p < 0.001$ *vs.* the model group), suggesting that ZnO@PDA exerted a potent anti-apoptotic effect in the PD model cells. To further explore the therapeutic mechanism of ZnO@PDA plus NIR irradiation in PD, we analyzed apoptosis-related proteins, inflammatory factors, and the key protein α-synuclein (α-syn) by western blotting. As illustrated in

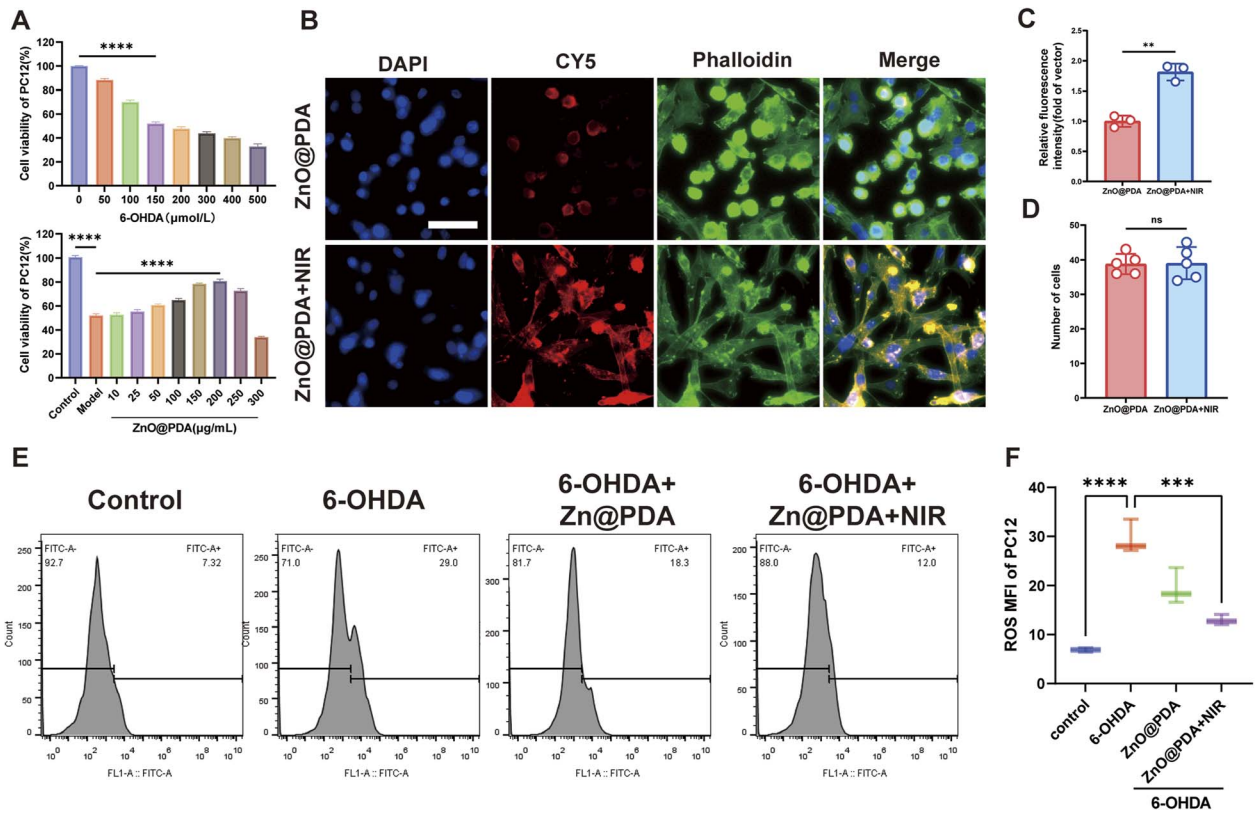

Fig. 2 *In vitro* validation of the functional properties of ZnO@PDA. (A) Cell viability assay of PC12 cells incubated with different concentrations of 6-OHDA and ZnO@PDA ($N = 4$, ****$p < 0.0001$). (B) Uptake of ZnO@PDA with or without NIR-mediated by PC12 cells (scale bars, 50 μm). (C) Quantitative fluorescence analysis of Cy5-labeled ZnO@PDA with or without NIR-mediated in Fig. 2B ($N = 3$, **$p < 0.01$). (D) Cell counting analysis of Cy5-labeled ZnO@PDA with or without NIR irradiation in Fig. 2B ($N = 5$, ns: not significant). (E) Flow cytometry analysis of ROS levels. (F) Quantitative analysis of ROS levels in Fig. 2E ($N = 3$, ***$p < 0.001$, ****$p < 0.0001$).

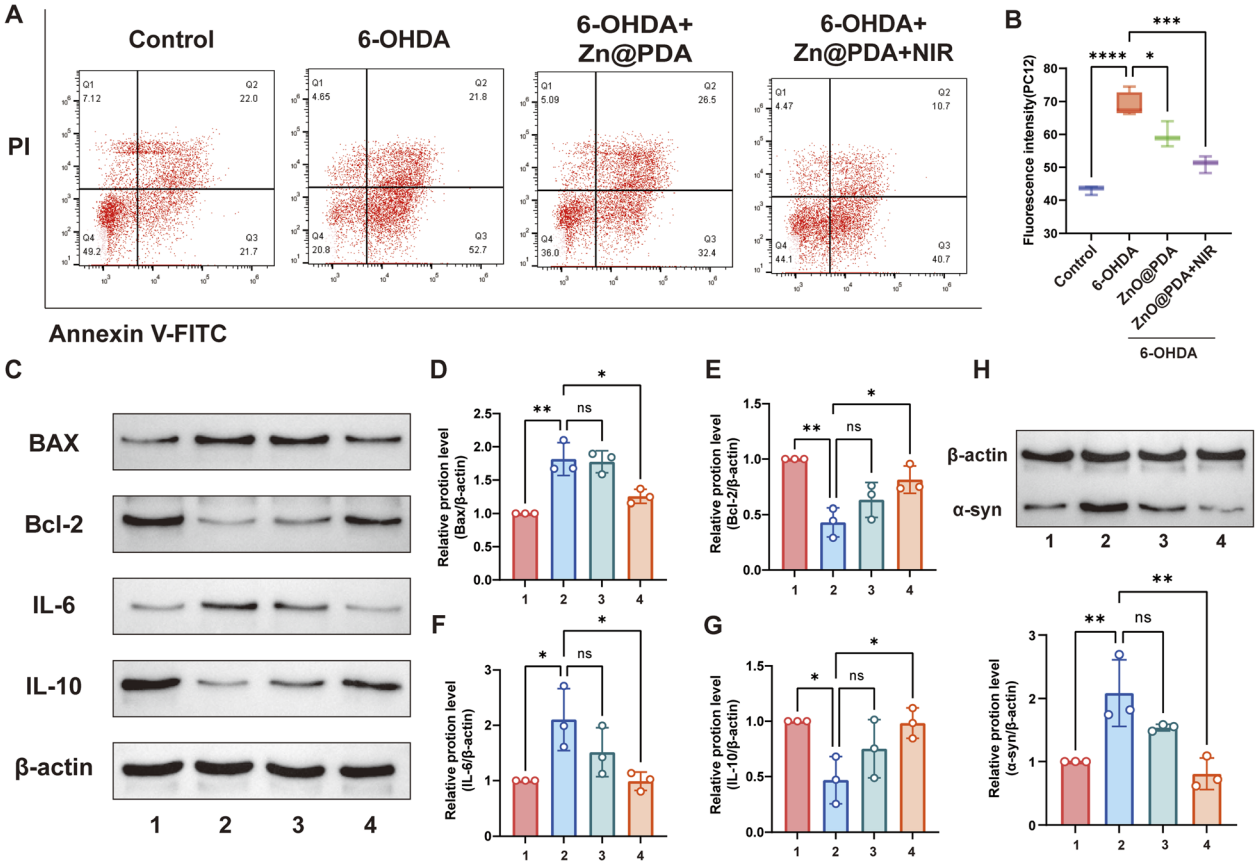

Fig. 3 *In vitro* validation of the molecular mechanism of ZnO@PDA for the treatment of PD. (A) Flow cytometry analysis of apoptosis. (B) Quantitative analysis of apoptosis in Fig. 3A ($N = 3$). (C) Western blotting of IL-6, IL-10, BAX, and Bcl-2 expression levels. Quantification of (D) BAX, (E) Bcl-2, (F) IL-6, and (G) IL-10 expression levels after different treatments. (H) Western blotting and quantification of α-syn expression levels after different treatments (1: control; 2: 6-OHDA; 3: ZnO@PDA; 4: ZnO@PDA + NIR; $N = 3$, ns: not significant, *$p < 0.05$, **$p < 0.01$, ***$p < 0.001$, ****$p < 0.0001$).

Fig. 3C–E, the model group exhibited upregulation of the pro-apoptotic protein Bax ($p < 0.01$) and downregulation of the anti-apoptotic protein Bcl-2 ($p < 0.01$). In contrast, ZnO@PDA + NIR treatment effectively reversed these changes, indicating an antiapoptotic state. Accumulating evidence has substantiated the presence of an inflammatory milieu in PD pathogenesis.[39,40] Our data showed a significant elevation of pro-inflammatory IL-6 ($p < 0.05$) concomitant with suppression of anti-inflammatory IL-10 ($p < 0.05$) in PD models, whereas ZnO@PDA + NIR intervention markedly attenuated this neuroinflammatory signature (Fig. 3F and G), demonstrating its potential for inflammatory modulation. It is well known that aberrant α-syn aggregation acted as a well-established pathological hallmark of PD.[41] Mechanistic studies have indicated that α-syn activates microglia, triggering pro-inflammatory cytokine release, and initiating neuroinflammatory cascades.[42] This vicious cycle of neuroinflammation and neurodegeneration progressively exacerbates the loss of dopaminergic neurons. Interestingly, our results confirmed that ZnO@PDA + NIR treatment significantly attenuated α-syn expression ($p < 0.01$; Fig. 3H). These results demonstrated that the combined treatment effectively suppressed pathological α-syn aggregation and modulated upstream oxidative stress and downstream neurodegenerative pathways.

2.4. *In vivo* experiments with ZnO@PDA

As a novel nanomaterial with clinical potential, a thorough biosafety evaluation of ZnO@PDA is imperative for identifying its *in vivo* toxicity and establishing appropriate therapeutic concentrations. Systematic dose-response studies in healthy mice revealed acute toxicity at higher doses (SI Fig. 3). Intravenous administration of ZnO@PDA at 1000, 500, and 250 mg kg^{-1} caused immediate mortality, whereas the 125 mg kg^{-1} dose resulted in delayed mortality within two hours post-injection, demonstrating clear dose-dependent toxicity. Histopathological analysis showed tissue damage in the liver, lungs, and spleen at doses exceeding 125 mg kg^{-1}, likely due to the inability of the body to properly metabolize such high NPs concentrations. Although the 62.5 mg kg^{-1} group exhibited minor organ toxicity relative to PBS controls, the complete absence of pathological abnormalities at 31.25 mg kg^{-1} conclusively established this as the maximum tolerated dose, providing a crucial safety benchmark for therapeutic development. Mechanistic investigation of the anti-PD efficacy of

ZnO@PDA revealed a previously unexpected sequential dependency between photothermal activation and US stimulation, which was the critical determinant for achieving noninvasive DBS.

Fig. 4A schematically illustrates the multi-modal protocol for ZnO@PDA + NIR + US combination treatment in murine models. Behavioral experiments demonstrated that laser-initiated administration (ZnO@PDA + NIR + US: NM + L + U) significantly alleviated impaired motor coordination in PD model mice compared to the US-preferred regimen (ZnO@PDA + US + NIR: NM + U + L), as evidenced by a significant reduction in total and steering time in the pole test ($p < 0.05$) (Fig. 4B and C) and a shortening of the time to traverse the balance beam ($p < 0.01$; Fig. 4D). Open-field behavioral tracking provided visual confirmation of these effects (Fig. 4E). Mice in the NM + U + L group displayed characteristic behaviors including reduced locomotion, increased corner preference, more frequent wall-hugging circling movements, and decreased center exploration. By contrast, the NM + L + U group maintained a nearly normal exploratory pattern. These behavioral metrics corroborated our *in vitro* findings, confirming that 808 nm laser pretreatment enhanced BBB permeability to facilitate targeted ZnO@PDA brain accumulation, enabling effective US-triggered neuromodulation—a continuous synergistic effect unattainable with US-first administration (NM + U + L).

Histopathological analysis by H&E staining revealed no abnormal morphological malformations in any of the major organs of the mice (Fig. 5A), which is consistent with previous toxicity experiments. Moreover, the excellent biocompatibility data confirmed that ZnO@PDA was suitable for *in vivo* biological applications. Brain histology showed densely packed neurons with a large cytosol, rounded nuclei, and distinct nucleoli in both the NM + L + U and control groups. Conversely, the NM + U + L and other treatment groups presented neuronal sparsity with occasional nuclear pyknosis and cytoplasmic shrinkage (Fig. 5B). Next, to better investigate the neurotherapeutic potential of ZnO@PDA under sequential laser-US irradiation in cerebral applications, we performed the following analyses. Nissl staining revealed differential neuroprotective patterns among treatment groups: the NM + L + U group maintained intact Nissl bodies with uniform cytoplasmic distribution, while the NM + U + L group showed neurodegenerative features, including partial Nissl body dissolution and characteristic neuronal degeneration morphology (Fig. 5C). Notably, immunofluorescence (IF) staining of the substantia nigra sections (Fig. 5D and E) revealed distinct treatment-dependent effects on dopaminergic markers. Briefly, the NM + U + L group exhibited pronouncedly reduced expression of both tyrosine hydroxylase (TH) ($p < 0.001$) and neurofilament (NF) ($p < 0.001$) compared to the NM + L + U group, whereas no significant difference was observed between the NM + L + U and normal control groups. These findings suggest that NM + L + U treatment successfully preserved neuronal structural integrity (as indicated by NF maintenance) and sustained dopaminergic functionality (as evidenced by the conserved TH level), which is essential for dopamine biosynthesis. In contrast, the NM + U + L group showed clear treatment failure, characterized by progressive degeneration of dopaminergic neurons, cytoskeletal disintegration (reduced NF), and impaired axonal transport mechanisms. Furthermore, neuroinflammatory profiling revealed striking differences between treatment modalities. The NM + U + L group displayed markedly elevated glial fibrillary acidicprotein (GFAP) expression ($p < 0.0001$ *vs.* NM + L + U; Fig. 5F), confirming robust astrocyte activation accompanied by the release of pro-inflammatory cytokines (IL-1β and TNF-α), which exacerbated neuronal damage. However, the NM + L + U group showed a substantial decrease in IL-1β, TNF-α, and IL-6 positive staining areas ($p < 0.001$; Fig. 5G–J), suggesting that laser pretreatment enhanced the BBB penetration of ZnO@PDA, thereby facilitating both free radical scavenging and cytokine modulation. This differential response explains the sustained pro-inflammatory state and poorer therapeutic outcomes in the NM + U + L group than in the neuroprotective effects achieved with NM + L + U group. Therefore, ZnO@PDA has established a precision-targeted paradigm for PD intervention that simultaneously addresses multiple pathological mechanisms.

3. Discussion

As the second most prevalent neurodegenerative disorder globally, PD is characterized by a progressive onset of motor symptoms, including postural instability, bradykinesia, and resting tremor, as well as non-motor complications such as cognitive decline, autonomic dysfunction and neuropsychiatric disturbances.[43,44] Pharmacological therapy remains the first-line intervention during the early stages of the disease. However, as the condition advances, a multidisciplinary approach involving neurosurgical and rehabilitative strategies becomes essential. DBS, a neuromodulatory technique with over three decades of clinical application, is currently the gold-standard surgical treatment for PD.[45] Despite its efficacy, the irreversible and invasive nature of DBS, along with the risk of complications, has spurred a growing interest in noninvasive alternatives.

Among these, NP-based therapeutics have emerged as a promising class of neuromodulatory agents, offering enhanced accessibility to neural tissues and potential for multifunctional integration.[46,47] Herein, we present a nanotechnological strategy that combines photothermally assisted BBB permeabilization with ultrasound-activated piezoelectric neuromodulation. To this end, we engineered a core–shell nanoplatform, ZnO@PDA, endowed with NIR-triggered photothermal conversion, US responsiveness, and ROS-scavenging capabilities. This multifunctional construct enabled spatiotemporally controlled neural stimulation while simultaneously mitigating oxidative stress, thereby addressing key challenges in the development of noninvasive neuromodulatory therapies for PD.

Successful construction of ZnO@PDA is imperative for therapeutic applications. Surface modification of ZnO NPs with PDA (Fig. 1A) induced a significant charge reversal from +32.52 mV (pristine ZnO) to −15.26 mV (ZnO@PDA). This surface electronegativity substantially improved the colloidal stability and extended *in vivo* circulation half-life (Fig. 1C) while

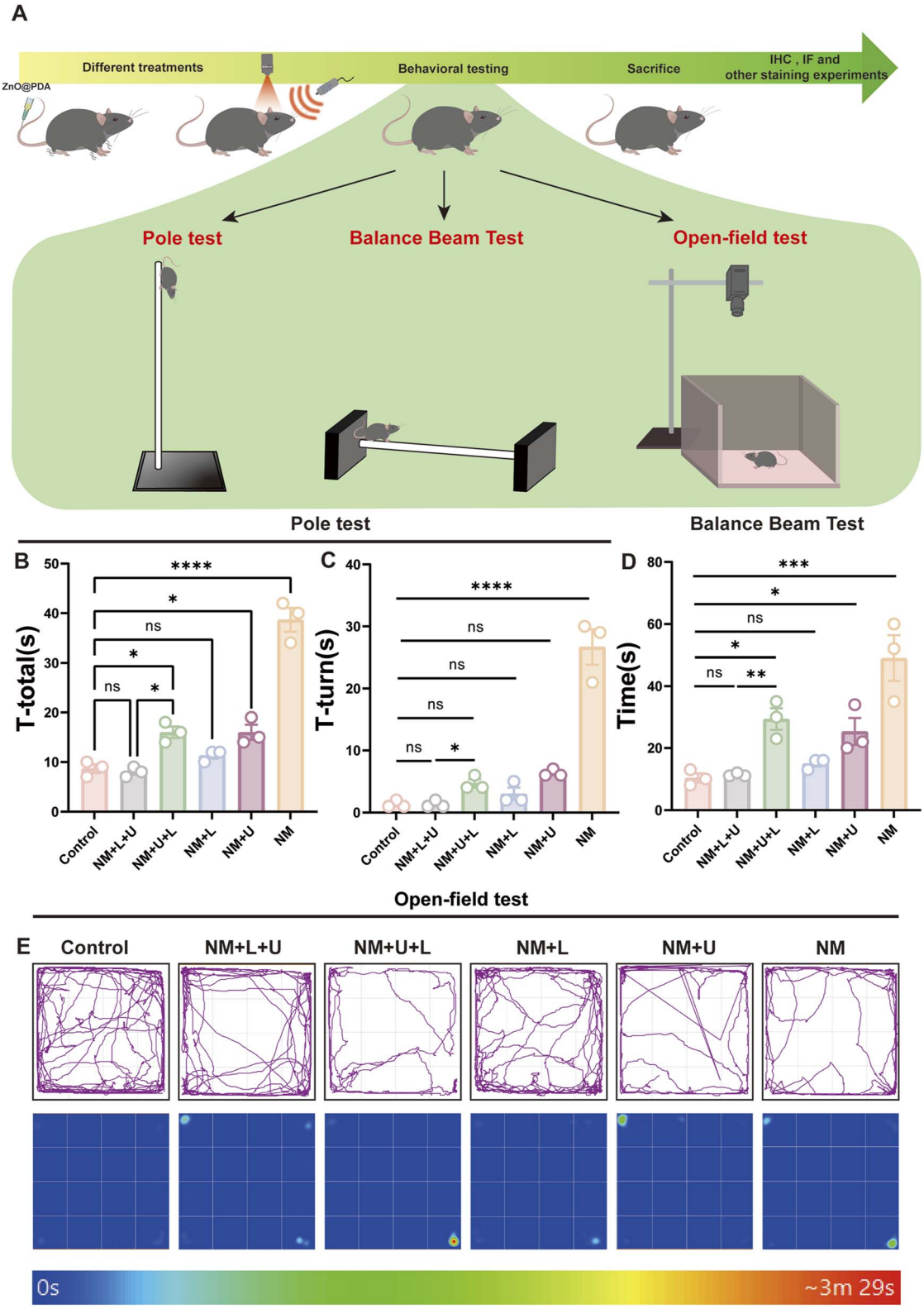

Fig. 4 Behavioral experiments after ZnO@PDA treatment in PD model mice. (A) Schematic diagram of ZnO@PDA *in vivo* therapeutic experimental flow and behavioral experiments. (B–E) The behavior assessment included various tests, including the (B and C) pole test, (D) balance beam test and (E) trajectory images and thermograms of open-field trials in PD model mice after different treatments ($N = 3$, ns: not significant, $^{*}p < 0.05$, $^{**}p < 0.01$, $^{***}p < 0.001$, $^{****}p < 0.0001$) (control: PBS; NM + L + U: ZnO@PDA + NIR + US; NM + U + L: ZnO@PDA + US + NIR; NM + L: ZnO@PDA + NIR; NM + U: ZnO@PDA + US; NM: ZnO@PDA).

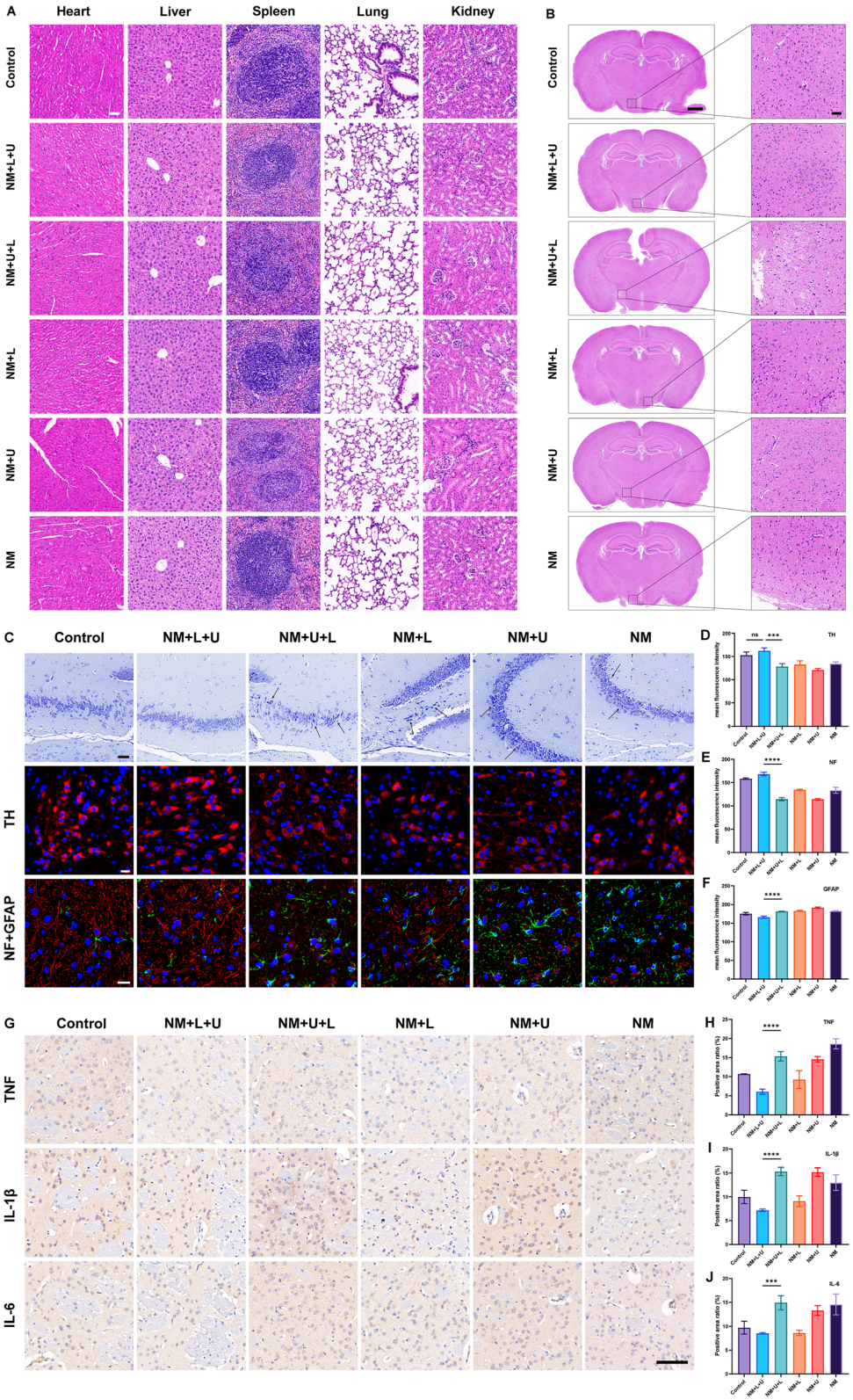

Fig. 5 Stained slides after *in vivo* treatment experiments. (A) H&E staining analysis of vital organs in six groups (scale bars, 50 μm). (B) Brain sections from six groups (left scale bars, 1000 μm. Right scale bars, 50 μm). (C) Nissl staining and immunofluorescence staining of TH, NF, and GFAP proteins in six groups (Nissl staining scale bars, 50 μm. IF scale bars, 20 μm). Quantitative analysis of mean fluorescence intensity of (D) TH, (E) NF, and (F) GFAP. (G) Immunohistochemistry of TNF, IL-1β and IL-6 in six groups (scale bars, 100 μm). Quantitative analysis of positive area ratio of (H) TNF, (I) IL-1β, and (J) IL-6. ($N = 3$, ns: not significant, ***$p < 0.001$, ****$p < 0.0001$) (control: PBS; NM + L + U: ZnO@PDA + NIR + US; NM + U + L: ZnO@PDA + US + NIR; NM + L: ZnO@PDA + NIR; NM + U: ZnO@PDA + US; NM: ZnO@PDA).

also enhancing the material affinity. Comprehensive material characterization, including TEM (Fig. 1E), elemental mapping, and XPS (Fig. 1G and H), confirmed the structural properties of ZnO@PDA with uniform PDA coating. XRD analysis (Fig. 1F) further verified the preservation of the ZnO crystal structure after the coating. This rationally engineered nanostructure demonstrated exceptional photothermal conversion efficiency, achieving a rapid temperature increase to 44 °C under 808 nm NIR irradiation (Fig. 1J). This precisely controlled mild hyperthermia contributes to reversible BBB permeabilization, facilitating targeted NPs accumulation in the cerebral parenchyma and creating optimal conditions for subsequent piezoelectric activation. Notably, stable current output (>0.12 μA) during 30 s US pulses (Fig. 1K) demonstrated robust piezoelectric properties. The above data confirmed that ZnO@PDA possesses optimal physicochemical properties for noninvasive DBS therapy. The spatiotemporal coordination of photothermal and piezoelectric effects enabled targeted "penetration–accumulation–activation" cascades with precise external energy guidance. Importantly, extended serum stability (72 h spectral integrity, SI Fig. 1) coupled with excellent biocompatibility (no observed toxicity at 31.25 mg kg^{-1}, SI Fig. 3) established a safety profile for translational applications. Furthermore, ZnO@PDA exhibited robust multi-targeted antioxidant activity, as evidenced by DPPH radical scavenging (Fig. 1L), TMB chromogenic assay (Fig. 1M) and $O_2^{\bullet-}$ neutralization (Fig. 1N). Its excellent chemo-functional properties enabled NPs to dynamically modulate IME after crossing the BBB, a capability further validated by subsequent *in vitro* cellular experiments.

In 6-OHDA-induced PC12 cell models, ZnO@PDA (200 μg mL^{-1}) under NIR radiation markedly downregulated the pro-inflammatory cytokine IL-6 and upregulated the anti-inflammatory cytokine IL-10 ($p < 0.05$, Fig. 3F and G). The effective reversal of the IL-6/IL-10 imbalance confirmed its anti-inflammatory regulatory function. Importantly, NIR-enhanced ZnO@PDA not only improved cellular uptake ($p < 0.01$, Fig. 2C) but also maintained cell viability with negligible cytotoxicity ($p > 0.05$, Fig. 2D), indicating high biocompatibility and efficient intracellular delivery. In addition, western blot analysis revealed the underlying neuroprotective mechanisms. Under NIR irradiation, ZnO@PDA substantially inhibited neuronal apoptosis by decreasing the pro-apoptotic Bax expression ($p < 0.05$, Fig. 3D) and increasing the anti-apoptotic Bcl-2 expression ($p < 0.05$, Fig. 3E). Concurrently, it markedly reduced α-syn aggregation ($p < 0.01$, Fig. 3H), suggesting that ZnO@PDA can intervene in the upstream pathological mechanisms of PD by mitigating protein misfolding.

In vivo experimental data have systematically demonstrated that BBB opening (laser-prioritized therapeutic sequence) is a critical prerequisite for achieving therapeutic efficacy in noninvasive DBS. Behavioral analyses revealed that the laser-first (NM + L + U) group exhibited near-normal motor function across multiple behavioral paradigms, including the pole-climbing test ($p < 0.05$ for total time *vs.* steering time, Fig. 4B and C), balance beam test ($p < 0.01$, Fig. 4D), and open-field assays (Fig. 4E and F). By contrast, the US-first (NM + U + L) group consistently displayed PD-like behavioral deficits. This sequence-dependent effect arose from laser preconditioning, wherein 808 nm laser irradiation induced localized hyperthermia (Fig. 1J), leading to transient and reversible BBB opening. This facilitated targeted enrichment of ZnO@PDA in the striatum, establishing a material foundation for subsequent US-triggered piezoelectric neuromodulation. Notably, reversing the treatment sequence caused peripheral NPs entrapment, which not only abolished therapeutic efficacy but also introduced potential systemic toxicity risks. Histopathological examination further corroborates the spatiotemporal precision of this approach. Brain sections from the NM + L + U group maintained neuronal density comparable to that of normal controls, with preserved Nissl body integrity and normal levels of TH and NF (Fig. 5D and E). Conversely, the NM + U + L group displayed a characteristic neurodegenerative pathology, including neuronal nuclear pyknosis, Nissl body dissolution, and significantly elevated GFAP expression ($p < 0.0001$, Fig. 5F), indicating a neuroinflammatory microenvironment driven by aberrant astrocyte activation. Additionally, this inflammatory cascade, driven by IL-1β/TNF-α release (Fig. 5G–J), exacerbated dopaminergic degeneration. Remarkably, the antioxidant properties of ZnO@PDA enabled selective ROS scavenging within the lesion area, following laser-mediated BBB penetration. Meanwhile, the US-triggered piezoelectric effect generates localized microcurrents that directly modulate the neuronal electrophysiological activity. This dual-modal "chemo-electrical" intervention targeted pivotal pathological nodes in PD, synergistically mitigating neuroinflammation and restoring neural circuit function, thus significantly enhancing the efficacy of noninvasive DBS.

4. Conclusion

In summary, the rational design and synthesis of the ZnO@PDA nanoplatform represent an innovative integration of photothermal transduction, piezoelectricity, and antioxidative capacity within a unified nanosystem, achieving multidimensional modulation of PD pathological microenvironments. In contrast to conventional DBS, this strategy employs a noninvasive approach for targeted NPs aggregation in the brain, followed by spatiotemporally precise therapy mediated by the intrinsic stimulus-responsive properties of the material. This sequential "penetration–accumulation–stimulation" framework not only offers a non-invasive alternative for PD management but also establishes a paradigm for nanomaterial-based interventions in other neurological disorders.

5. Materials and methods

5.1. Synthesis of ZnO@PDA and PDA

To prepare ZnO@PDA, 20 mg of ZnO NPs were evenly dissolved in water, 5 mg of dopamine hydrochloride was added, and the mixture was continuously stirred at room temperature. The pH was adjusted to 12–13 using aqueous ammonia, and the reaction proceeded for 3 h under continuous stirring. The product was centrifuged, washed, and dried to obtain black ZnO@PDA.

PDA was prepared by dissolving 20 mg dopamine hydrochloride in 20 mL of ethanol, and the pH was adjusted to 13–14 using ammonia. After 2 h, a dark-black solution was formed. The product was dialyzed to neutrality and freeze-dried to yield PDA powder.

5.2. Physicochemical characterization

The synthesized materials (ZnO, PDA, and ZnO@PDA) were characterized for their size, surface charge, optical properties, chemical structure, crystallinity, and morphology. Techniques included dynamic light scattering (DLS), UV-Vis spectroscopy, Fourier-transform infrared spectroscopy (FTIR), X-ray diffraction (XRD), X-ray photoelectron spectroscopy (XPS), and transmission electron microscopy (TEM). Detailed characterization methods and instrument parameters are described in the SI (SI, Section S1.1).

5.3. Stability and photothermal conversion property

The stability of ZnO@PDA was assessed by monitoring the absorption peak intensity over 72 h using UV-Vis spectroscopy. PBS solutions of ZnO@PDA with concentrations ranging from 50 to 400 μg mL^{-1} were prepared for this study. Each solution was exposed to an 808 nm laser (power density: 1.5 W cm^{-2}) for 20 min. Temperature changes were recorded both during irradiation and during the subsequent cooling phase to room temperature to evaluate photothermal conversion efficiency.

5.4. ROS scavenging activity of ZnO@PDA

The reactive oxygen species (ROS) scavenging capacity of ZnO@PDA was assessed using three distinct assays targeting DPPH radicals, hydroxyl radicals ($^{\bullet}OH$), and superoxide anions ($O_2^{\bullet-}$). Absorbance measurements were used to quantify the scavenging activity. Full experimental details for each assay are provided in the SI (Section S1.2).

5.5. US piezoelectric property

ZnO@PDA (10 mg) was dispersed in anhydrous ethanol (1 mL) and mixed with 10 μL Nafion. The resulting suspension was drop-cast onto a glassy carbon electrode and dried in a forced air oven at 55 °C. Electrochemical tests were performed using an electrochemical workstation (ChI660E) with a standard three-electrode configuration: the sample served as the working electrode, a saturated calomel electrode was the reference electrode, and a platinum electrode was the counter electrode, with 0.1 M Na_2SO_4 as the electrolyte. During electrochemical testing, the system was subjected to US irradiation (frequency: 40 kHz, power: 180 W, intensity: 1.8 W cm^{-2}) while monitoring the current response.

5.6. Assessing cell viability

PC12 cells were seeded in 96-well plates. To establish a model, cells were treated with 6-OHDA (0–500 μmol L^{-1}) for 24 h. Cell viability was assessed using the CCK-8 assay, with absorbance measured at 450 nm. The 6-OHDA concentration inducing ~50% cell death was selected for subsequent experiments. To evaluate protection, cells were pretreated with ZnO@PDA (10–300 μg mL^{-1}) for 6 h prior to 24 h 6-OHDA exposure, followed by the CCK-8 assay. The ZnO@PDA concentration yielding maximal cytoprotection was selected for further studies. Detailed procedures are provided in SI (Section S1.3).

5.7. Cellular uptake assay

PC12 cells were seeded in 12-well plates. Cells were treated with Cy5-ZnO@PDA (150 μg mL^{-1}) with or without concurrent NIR irradiation (808 nm, 0.3 W cm^{-2}, 5 min) for 1 h. After treatments, cells were fixed, stained with phalloidin and DAPI, and visualized using confocal fluorescence microscopy. Detailed procedures are provided in SI (Section S1.4). Fluorescence stability was evaluated (Fig. S4–6).

5.8. Flow cytometry assays

PC12 cells were seeded in 6-well plates and divided into four groups: control, 6-OHDA, 6-OHDA + ZnO@PDA, and 6-OHDA + ZnO@PDA + NIR (808 nm, 0.3 W cm^{-2}, 5 min). After 12 h of treatment, cells were harvested, stained with CM-H2DCFDA (10 μmol L^{-1}, 30 min), and analyzed by flow cytometry. Mean fluorescence intensity was quantified for each group ($n = 3$). Detailed procedures are provided in SI (Section S1.5).

5.9. Cell apoptosis detection

PC12 cells were allocated to four treatment groups as previously described. Cells were harvested, stained with Annexin V-FITC and propidium iodide (PI) using an apoptosis detection kit, and analyzed by flow cytometry within 30 min. Detailed procedures are provided in SI (Section S1.6).

5.10. Western blotting

For *in vitro* experiments, the cells were divided into four groups. Following cell harvesting, proteins were extracted and subjected to western blot analysis as previously described.[48] Membranes were probed with the following primary antibodies: anti-Bcl-2 (1:2000), anti-BAX (1:2000), anti-IL-10 (1:2000), anti-IL-6 (1:500), and anti-α-syn (1:1000). Protein expression levels were quantified using the ImageJ software, and three independent experiments were performed for each experimental group.

5.11. Animal experiments

All animal experiments were approved by the Ethics Committee of the Guangdong Provincial People's Hospital (protocol no. KY2024-207-02), and performed in accordance with the guide for the care and use of laboratory animals (National Research Council) and ARRIVE guidelines.

C57BL/6J mice were used in this study; details of animal procurement, housing, and care are provided in SI. To establish the PD model, mice were intraperitoneally injected with 1-methyl- 4-phenyl-1, 2, 3, 6-tetrahydropyridine (MPTP) (18 mg kg^{-1}) four times daily at 2-hour intervals for seven consecutive days, and the experimental procedures were performed as previous literature.[32]

5.12. Acute toxicity test

Healthy mice were randomly allocated into 12 groups: a PBS control group ($n = 3$) and 11 groups treated with different concentrations of ZnO@PDA ($n = 3$ per group, received 0.183–200.00 mg mL^{-1} concentrations *via* tail vein injection). After 24 h of drug administration, all mice were anesthetized with 0.25 mL tribromoethanol *via* intraperitoneal injection and euthanized by cervical dislocation. Survival status, gross organ morphology, and histopathological results were recorded.

5.13. *In vivo* therapy

Fifteen PD model mice were randomly divided into five groups ($n = 3$ per group) and treated with intravenous ZnO@PDA (0.1 mL, 1 mg mL^{-1}) every three days for 30 days. The experimental groups were ZnO@PDA + NIR + US (NM + L + U), ZnO@PDA + US + NIR (NM + U + L), ZnO@PDA + NIR (NM + L), ZnO@PDA + US (NM + U), and ZnO@PDA only (NM). Following administration, the experimental groups received laser and/or ultrasound treatment (808 nm NIR, 1.0 W cm^{-2}, 5 min; ultrasound, 10 min) 30 minutes post-injection, according to the previously defined protocols. This treatment regimen was repeated for all groups 4 hours post-administration. Three healthy mice were randomly selected as the controls. Detailed procedures are provided in SI (Section S1.7).

5.14. Behavioral assessment of mice after treatment

Open-field test: prior to testing, mice were acclimated to the experimental room for 30 min to minimize stress. Each subject was then placed in a 45 × 45 × 45 cm square area and allowed to explore freely for 10 min. Their movement trajectories, total distance, immobile time, and center zone duration/entries were recorded using an ANY-maze tracking system.

Rotarod test: the mice were positioned on the rotarod. Two evaluation methods were tested: rotation at a fixed speed of 15 rpm and acceleration from 4 to 40 rpm for 100 s. The time during which each mouse remained on the rod was recorded by using a rotarod apparatus.

Pole test: mice were placed head-up on a vertical pole with a rough surface (70 cm tall, 1 cm diameter). The time required for mice to turn around (t-turn) and climb to the bottom of the pole (t-total) was recorded.

5.15. IF staining

Brain sections were dewaxed and subjected to heat-induced antigen retrieval using EDTA (pH 9.0). After blocking, the sections were incubated with primary antibodies against TH (dilution 1:1000), NF (dilution 1:500), and GFAP (dilution 1:800). Following PBS washes to remove unbound antibodies, fluorescently labeled secondary antibodies were applied. After additional washes, DAPI was used for nuclear staining. Quantification was performed using threshold-based analysis.

5.16. Immunohistochemistry (IHC)

Dewaxed brain sections were subjected to heat-mediated antigen retrieval and blocked with 5% normal goat serum. The slides were incubated overnight at 4 °C with primary antibodies against IL-6 (dilution, 1:200), IL-1β (dilution, 1:100), and TNF-α (dilution, 1:300). After washing with PBS to remove the unbound primary antibodies, secondary antibodies (dilution, 1:1000) were added and incubated for 1 h. Subsequently, a chromogenic substrate was applied. Images were acquired using a light microscope (or slide scanner), and positive staining was quantified by ImageJ.

5.17. H&E staining

After treatment, the major organs (heart, liver, spleen, lung, kidney, and brain) were collected from the six groups (including normal control) of mice, fixed in 4% paraformaldehyde, and sectioned. H&E staining was performed according to standard procedures. Images were captured using the 3D HISTECH Pannoramic 250 (3DHISTECH, Hungary).

5.18. Statistical analysis

The experimental data are presented as the mean ± standard deviation (SD) with biological replicates ($n \geq 3$). Intergroup comparisons were performed using student's *t*-test for two experimental groups or one-way ANOVA followed by appropriate post hoc tests for multiple group comparisons. All statistical analyses and data visualization were conducted using GraphPad Prism 9.0 software (GraphPad Software, Inc).

Ethics approval and consent to participate

All animal procedures were approved by the Research Ethics Committee of Guangdong Provincial People's Hospital (KY2024-207-02) and performed in accordance with the Guide for the Care and Use of Laboratory Animals (National Research Council) and ARRIVE guidelines.

Author contributions

Conceptualization: Jianhua Liu, Xiazi Huang, Wenting Shang. methodology: Yingfeng Tu, Xueer Xia, investigation: Meiyin Lin, Yu Chen, Zirong Zhang. visualization: Xueer Xia, Jianbang Han, Xin Li. formal analysis: Jianbang Han. supervision: Bin Liu, Yingfeng Tu, Shuai Han. data curation: Meiyin Lin, Yue Zheng. writing—original draft: Xueer Xia, Wenting Shang, Jianhua Liu. writing—review & editing: Xiazi Huang, Wenting Shang, Jianhua Liu.

Conflicts of interest

The authors declare that they have no conflict of interest.

Data availability

All data from the study period are available in the main text or supplementary information (SI). Supplementary information: additional figures showing dose–response curves, and

supplementary methods for the synthesis of key compounds. See DOI: https://doi.org/10.1039/d5ra07719b.

Acknowledgements

This work was supported by grants from the National Natural Science Foundation of China (Grant No. 81971680), Research Start-up Funds for the National Natural Science Foundation of China (Grant No. 8217050958, 8217111167, 8237110140), Ganzhou Municipal Science and TechnologyKey Program (Grant No. 2023LNS26875), and Excellent Scientific Research Project (Grant No. YCKY2024-0100221002).

References

1 T. Kamath, *et al.*, Single-cell genomic profiling of human dopamine neurons identifies a population that selectively degenerates in Parkinson's disease, *Nat. Neurosci.*, 2022, **25**, 588–595.
2 S. M. Goldman, Environmental toxins and Parkinson's disease, *Annu. Rev. Pharmacol. Toxicol.*, 2014, **54**, 141–164.
3 E. R. Dorsey, T. Sherer, M. S. Okun and B. R. Bloem, The Emerging Evidence of the Parkinson Pandemic, *J. Parkinsons Dis.*, 2018, **8**, S3–S8.
4 B. R. Bloem, M. S. Okun and C. Klein, Parkinson's disease, *Lancet*, 2021, **397**, 2284–2303.
5 V. Hvingelby, *et al.*, Directional deep brain stimulation electrodes in Parkinson's disease: meta-analysis and systematic review of the literature, *J. Neurol., Neurosurg. Psychiatry*, 2025, **96**, 188–198.
6 V. Sisodia, *et al.*, Bidirectional Interplay between Deep Brain Stimulation and Cognition in Parkinson's Disease: A Systematic Review, *Mov. Disord.*, 2024, **39**, 910–915.
7 C. Cheyuo, *et al.*, Comprehensive characterization of intracranial hemorrhage in deep brain stimulation: a systematic review of literature from 1987 to 2023, *J. Neurosurg.*, 2024, **141**, 381–393.
8 J. Tiefenbach, *et al.*, Intracranial Bleeding in Deep Brain Stimulation Surgery: A Systematic Review and Meta-Analysis, *Stereotact. Funct. Neurosurg.*, 2023, **101**, 207–216.
9 X. Jia, J. Li, W. Zhang, J. Wei and Y. Zhang, Therapeutic Measures for Infections Originating from Scalp Incisions Following Deep Brain Stimulation in Patients with Parkinson's Disease, *World Neurosurg.*, 2024, **192**, e134–e138.
10 B. Wu, *et al.*, Delayed-onset seizures after subthalamic nucleus deep brain stimulation surgery for Parkinson's disease, *J. Clin. Neurosci.*, 2024, **124**, 81–86.
11 A. J. Fenoy and R. J. Simpson, Risks of common complications in deep brain stimulation surgery: management and avoidance, *J. Neurosurg.*, 2014, **120**, 132–139.
12 E. J. Boviatsis, L. C. Stavrinou, M. Themistocleous, A. T. Kouyialis and D. E. Sakas, Surgical and hardware complications of deep brain stimulation. A seven-year experience and review of the literature, *Acta Neurochir.*, 2010, **152**, 2053–2062.
13 T. M. Ellis, *et al.*, Reoperation for suboptimal outcomes after deep brain stimulation surgery, *Neurosurgery*, 2008, **63**, 754–760.
14 M. S. Okun, *et al.*, Subthalamic deep brain stimulation with a constant-current device in Parkinson's disease: an open-label randomised controlled trial, *Lancet Neurol.*, 2012, **11**, 140–149.
15 R. Beisteiner, A. Lozano, V. Di Lazzaro, M. S. George and M. Hallett, Clinical recommendations for non-invasive ultrasound neuromodulation, *Brain-Stimul.*, 2024, **17**, 890–895.
16 H. R. Siebner, *et al.*, Transcranial magnetic stimulation of the brain: What is stimulated? - A consensus and critical position paper, *Clin. Neurophysiol.*, 2022, **140**, 59–97.
17 S. Alfihed, *et al.*, Non-Invasive Brain Sensing Technologies for Modulation of Neurological Disorders, *Biosensors*, 2024, **14**(7), 335.
18 T. Kim, *et al.*, Deep brain stimulation by blood-brain-barrier-crossing piezoelectric nanoparticles generating current and nitric oxide under focused ultrasound, *Nat. Biomed. Eng.*, 2023, **7**, 149–163.
19 J. Wu, *et al.*, A nanoparticle-based wireless deep brain stimulation system that reverses Parkinson's disease, *Sci. Adv.*, 2025, **11**, o4927.
20 K. S. Tang, W. See and R. Naidu, Neuroprotective properties of zinc oxide nanoparticles: therapeutic implications for Parkinson's disease, *Biosci. Rep.*, 2024, **44**(11), BSR20241102.
21 M. Jin, *et al.*, Toxicity of different zinc oxide nanomaterials and dose-dependent onset and development of Parkinson's disease-like symptoms induced by zinc oxide nanorods, *Environ. Int.*, 2021, **146**, 106179.
22 X. Dong-Chen, C. Yong, X. Yang, S. Chen-Yu and P. Li-Hua, Signaling pathways in Parkinson's disease: molecular mechanisms and therapeutic interventions, *Signal Transduction Targeted Ther.*, 2023, **8**, 73.
23 H. R. Morris, M. G. Spillantini, C. M. Sue and C. H. Williams-Gray, The pathogenesis of Parkinson's disease, *Lancet*, 2024, **403**, 293–304.
24 J. Hu, *et al.*, Polydopamine free radical scavengers, *Biomater. Sci.*, 2020, **8**, 4940–4950.
25 X. Bao, J. Zhao, J. Sun, M. Hu and X. Yang, Polydopamine Nanoparticles as Efficient Scavengers for Reactive Oxygen Species in Periodontal Disease, *ACS Nano*, 2018, **12**, 8882–8892.
26 Z. Lv, Y. Zeng, T. Lv, Q. Liu and L. Han, GRP94 mediates blood–brain barrier permeation and substantia nigra-specific drug distribution in Parkinson's disease, *Colloids Surf., B*, 2025, **250**, 114585.
27 K. Xu, *et al.*, Engineered Selenium/Human Serum Albumin Nanoparticles for Efficient Targeted Treatment of Parkinson's Disease via Oral Gavage, *ACS Nano*, 2023, **17**, 19961–19980.
28 L. Gong, *et al.*, Carbon nitride-based nanocaptor: An intelligent nanosystem with metal ions chelating effect for enhanced magnetic targeting phototherapy of Alzheimer's disease, *Biomaterials*, 2021, **267**, 120483.

29 Y. Liu, *et al.*, Near-Infrared Radiation-Assisted Drug Delivery Nanoplatform to Realize Blood–Brain Barrier Crossing and Protection for Parkinsonian Therapy, *ACS Appl. Mater. Interfaces*, 2021, **13**, 37746–37760.
30 H. Cheng, *et al.*, Synergistic photothermal and chemo-therapeutic platform utilizing Cu(2-x)Se/PDA/AIPH nanoparticles for targeted tumor eradication, *Biomater. Adv.*, 2025, **169**, 214196.
31 Y. Fu, *et al.*, Polydopamine antibacterial materials, *Mater. Horiz.*, 2021, **8**, 1618–1633.
32 Y. Gao, *et al.*, NIR-Assisted MgO-Based Polydopamine Nanoparticles for Targeted Treatment of Parkinson's Disease through the Blood–Brain Barrier, *Adv. Healthcare Mater.*, 2022, **11**, e2201655.
33 Y. Xiang, *et al.*, Rapid and Superior Bacteria Killing of Carbon Quantum Dots/ZnO Decorated Injectable Folic Acid-Conjugated PDA Hydrogel through Dual-Light Triggered ROS and Membrane Permeability, *Small*, 2019, **15**, e1900322.
34 J. Xue, W. Zheng, L. Wang and Z. Jin, Scalable Fabrication of Polydopamine Nanotubes Based on Curcumin Crystals, *ACS Biomater. Sci. Eng.*, 2016, **2**, 489–493.
35 A. Irshad, *et al.*, Unveiling the power of TiO(2) doped ZnO nanomaterial as an effective antimicrobial solution in the leather industry, *Heliyon*, 2024, **10**, e38414.
36 M. A. Burguillos, *et al.*, Caspase signalling controls microglia activation and neurotoxicity, *Nature*, 2011, **472**, 319–324.
37 E. Lazdon, N. Stolero and D. Frenkel, Microglia and Parkinson's disease: footprints to pathology, *J. Neural Transm.*, 2020, **127**, 149–158.
38 Y. Lee, S. Lee, S. C. Chang and J. Lee, Significant roles of neuroinflammation in Parkinson's disease: therapeutic targets for PD prevention, *Arch Pharm. Res.*, 2019, **42**, 416–425.
39 C. Zhang, *et al.*, Engineered Extracellular Vesicle-Based Nanoformulations That Coordinate Neuroinflammation and Immune Homeostasis, Enhancing Parkinson's Disease Therapy, *ACS Nano*, 2024, **18**, 23014–23031.
40 J. E. Park, Y. H. Leem, J. S. Park, S. E. Kim and H. S. Kim, Astrocytic Nrf2 Mediates the Neuroprotective and Anti-Inflammatory Effects of Nootkatone in an MPTP-Induced Parkinson's Disease Mouse Model, *Antioxidants*, 2023, **12**(11), 1999.
41 S. Ray, *et al.*, α-Synuclein aggregation nucleates through liquid-liquid phase separation, *Nat. Chem.*, 2020, **12**, 705–716.
42 Y. Li, *et al.*, Targeting Microglial α-Synuclein/TLRs/NF-kappaB/NLRP3 Inflammasome Axis in Parkinson's Disease, *Front. Immunol.*, 2021, **12**, 719807.
43 L. Trevisan, *et al.*, Genetics in Parkinson's disease, state-of-the-art and future perspectives, *Br. Med. Bull.*, 2024, **149**, 60–71.
44 P. D. N, *et al.*, Neuroprotective role of coconut oil for the prevention and treatment of Parkinson's disease: potential mechanisms of action, *Biotechnol. Genet. Eng. Rev.*, 2024, **40**, 3346–3378.
45 R. Rajan, K. Garg, A. K. Srivastava and M. Singh, Device-Assisted and Neuromodulatory Therapies for Parkinson's Disease: A Network Meta-Analysis, *Mov. Disord.*, 2022, **37**, 1785–1797.
46 Q. Zheng, *et al.*, Ameliorating Mitochondrial Dysfunction of Neurons by Biomimetic Targeting Nanoparticles Mediated Mitochondrial Biogenesis to Boost the Therapy of Parkinson's Disease, *Adv. Sci.*, 2023, **10**, e2300758.
47 H. Hernández-Parra, *et al.*, Repositioning of drugs for Parkinson's disease and pharmaceutical nanotechnology tools for their optimization, *J. Nanobiotechnol.*, 2022, **20**, 413.
48 J. Liu, *et al.*, PLEK2 and IFI6, representing mesenchymal and immune-suppressive microenvironment, predicts resistance to neoadjuvant immunotherapy in esophageal squamous cell carcinoma, *Cancer Immunol., Immunother.*, 2023, **72**, 881–893.